Removal Mechanism of Abrasive Jet Polishing with a Novel Nozzle

Qiaoling YUAN[1, 2], Xun CHEN[2] and Donghui WEN[1]

[1] Key Laboratory of Special Purpose Equipment and Advanced Manufacturing Technology of Ministry of Education, Zhe-jiang University of Technology, Hang-zhou, 310014, China
[2]General Engineering Research Institute, Faculty of Engineering and Technology, Liverpool John Moores University, Liverpool, L3 3AF, UK

X.Chen@ljmu.ac.uk

Abstract. In view of the high-precision and low-damage requirements for surface polishing of hard and brittle components, an abrasive jet polishing process using a novel nozzle with specifically designed shroud was proposed. The removal mechanism of abrasive jet polishing was investigated by simulating the jet flow in the interaction area of the nozzle shroud and workpiece. The simulation results indicate that the velocity of the abrasive jet increases greatly by the shroud and the direction of the jet is aligned almost parallel to the workpiece surface. With such a design, the normal force of the abrasive jet is minimized to reduce the impact damage of the workpiece surface. Further, the stabilized abrasive jet insures a smooth machining. The machining experiments were performed on the quartz glass component, a typical hard and brittle material. The results of the shrouded abrasive jet polishing experiments show that the material removal mainly relied on the shearing and scratching of the workpiece surface rather than the mechanical shock impacts, which is consistent with the simulation findings.

Keywords: abrasive jet machining; Nozzle; K9 optic glass; removal mechanism.

1 Introduction

Along with the development of in the fields of aerospace, automobile, new energy, optics and medicine, the increasing use of hard and brittle materials, such as optical glass, optical crystals, and engineering ceramics, etc., for the functional surface of products has led to significant challenges for the precision machining technology. A high-precision , extremely smooth and intact surface is an essential requirement for high optical resolution, reduction of scattering loss, enhancement of damage-resistance threshold, and the guarantee of a reliable performance for a critical precision application that demands geometrical accuracy and surface integrity quality at the same time[1-3]. Moreover, the machining efficiency of parts need to be elevated due to the large sizes of the finished products including large-calibre space mirrors, laser optical components, etc., and the high-quantity demands (such as the aspherical lens, etc.). Accordingly, to meet the high machining requirements of the sculptured surface parts of hard and brittle materials, a super-precision machining technique with higher degree of accuracy, better integrity quality and production efficiency is highly desirable.

In 1992, when performing smoothing studies on the extremely hard and rough surface of diamond thin-films, Hashis[4, 5] found that the workpieces were cut or micro-cut more effectively by the ejective abrasive particles along the tangential direction rather than along the perpendicular direction with a small incidence angle between the injection direction of the jet and the normal direction. Accordingly, in 1998, Fahnle[6, 7] developed a low-pressure micro-abrasive jet ejected by a nozzle in a controllable way and then adopted to impose impacts on the workpieces. The surface quality of the complex aspherical optical components was therefore improved significantly. Similar experiments were performed by Booij [8, 9], who concluded that improved surface shapes could be obtained by adjusting the movement trails of the nozzle. In Messelink's work[10], a micro-abrasive jet was used to perform polishing machining on a spherical surface. Abrasive water jet machining was applied to process glass/epoxy composite laminates and the polishing process was modelled by CFD[11, 12].

The feasibility of polishing complex surface of hard and brittle materials parts by abrasive jet has been improved upon in the studies described above; however, some problems remain to be overcome such as the nozzle wear, the divergent of jets, and the impact damages to jets[13-15].The processing schematic diagram of traditional abrasive jet polishing is shown in Figure 1. In this paper, a constraint abrasive jet polishing (C-AJP) method was put forward. The formation mechanism of the abrasive jet was designed and directed restrict by the polishing tool head shroud so that the abrasive jet flows parallel to the surface. The abrasive jet was constrained shifting along the workpiece surface and exiting the slit gap, making almost all applied abrasive force on the workpiece surface transformed into tangential shearing stress. As a result, such a polishing process mainly depends on the shearing and scratching on the surface rather than mechanical impact, which not only decreases of impact damages, but also enhances polishing precision and efficiency. Moreover, a slender nozzle in the jet was no longer a necessity, and the costs could be greatly reduced by the cyclic utilization of the abrasive jet; this was also beneficial by reducing environmental pollution.

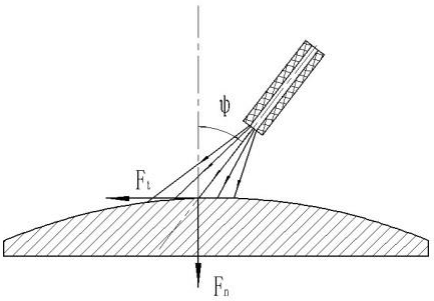

Figure1. Schematic diagram of traditional jet polishing.

2 The structure of the novel polishing nozzle

In order to generate an abrasive flow along the workpiece surface, a polishing tool head is designed and manufactured. The design sketch is presented in Figure 2, where F is the preload force and α is the inject angle. The head is designed as a replaceable module and is capable to match up with different shapes of workpieces. Wear-resistant elastic materials, such as nylon and polyurethane, were chosen in order to achieve a uniform contact between the tool head and workpiece surface and to improve the abrasion resistance of the tool head.

The polishing tool head was pressed on the workpiece surface before polishing. When the pressure of the abrasive flow in the tool was higher than the force given by the preload module, the tool head raised and abrasive jets formed along the gap between the bottom surface of the tool head and the workpiece surface. Through the polishing tool head, the abrasive flow changes its direction from normal to work surface into a tangential jet under the action of the restraint module. Precision polishing was accomplished by controlling the dwelling time of the polishing tool and the volume of the abrasive flow.

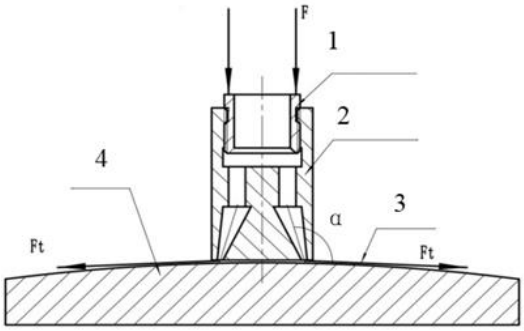

1 Nozzle, 2 shroud, 3 jet, 4 workpiece

Figure 2. Polishing schematic of the abrasive jet with specified nozzle.

The dimensions of polishing tool head design are shown in Figure 3 as a model for the simulation analysis of nozzle performance. The outer diameter of the tool head D_0 = 36mm, the inner diameter of the inlet section D_1 = 28mm, the inner diameter of the annular outlet D_2 = 28 mm and the outer diameter of the annular outlet D_3 = 32mm. The length of shunt section L_2 = 12mm and a slightly longer longitudinal length L_1 = 16mm is designed at the exit section, so that an abrasive flow can be fully developed to when the jet flowing from the shunt section to the exit section.

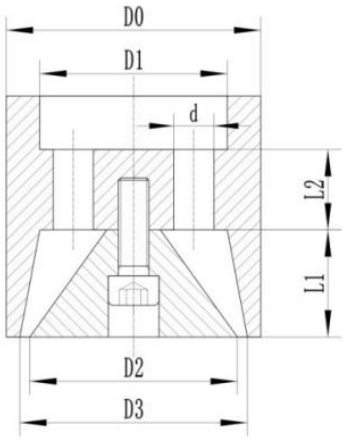

Figure3. Mechanical model of the simulation part.

The polishing tool has 8 separated channel holes in the middle part. The diameters of these channel holes are *d = 6 mm*,

$$A_M = 8\pi\left(\frac{d}{2}\right)^2 = 72\pi(mm^2) \quad (1)$$

The velocity and pressure of jet should be improved by the special polishing tool, so the area of the annular section A_{Out} should less than the sum of the base area of eight cylinders A_M.

$$A_{Out}=\pi\left(\frac{D_3}{2}\right)^2-\pi\left(\frac{D_2}{2}\right)^2 \quad (2)$$

So A_{Out} = 60 mm^2, the inlet cross section is larger than the outlet one, which will ensure a stable flow in the tool head.

3 Simulation

3.1 Abrasive flow modelling

During polishing, the abrasive flow passes through the designed nozzle forming a plane jet. It is an incompressible low viscosity two-phase flow with scattered flouting abrasive particles. The liquid density of the abrasive flow ρ_l is 1134.8 kg/m^3, the solid density of the abrasive flow ρ_s is 3170 kg/m^3,

the volume fraction of the abrasive is 15%, so the ρ of the two-phase abrasive flow is 1440 kg/m^3. The viscosity μ of the abrasive flow is 2.355 $mPa{\cdot}s$ measured from the experiment.

The Reynolds number at the nozzle can be calculated by:

$$Re_0 = \frac{v_0 d_H}{\nu} \tag{3}$$

In Eq. (3), v_0 is the velocity of the jet; based on the internal flow rate calculation, v_0=11m/s. The d_H is the Hydraulic diameter.

$$d_H = 4\frac{A_{Out}}{S} \tag{4}$$

where S is the perimeter of the cross-section of the fluid contact to solid region.

$$S = \frac{1}{2}\pi(D_2 + D_3) = 30\pi \tag{5}$$

So the d_H=8mm.

ν is the kinematic viscosity of the abrasive flow. .

$$\nu = \frac{\mu}{\rho} = 1.635\times10^{-6} m^2/s \tag{6}$$

Therefore the Reynolds number can be calculated as Re_0 =53823.

The internal flow of the jet usually is a turbulent jet according to the engineer experience, when Re_0 > 8000.

In order to make the Reynolds equations solvable, the unknown correlation term in the Reynolds equations or in the transport equations of the turbulent characteristics expressed by the term of the low order correlation or the time average. The jet flow in the near wall region is a kind of low Reynolds number turbulence as the effects of the wall and the viscous of the flow, the various scales of turbulence, as well as the characteristics of transport and dissipation are different from the fully developed turbulence, that showing a fairly inhomogeneous and anisotropic. So the calculation accuracy of the standard $k-\varepsilon$ model isn't high enough in the near wall region. The SST (Menter's Shear Stress Transport) turbulence model which use a low Reynolds number $k-\omega$ mode in near wall region was proposed. The standard k-ε model only applied at the end of the external flow zone and the free shear layers[16, 17] . A smooth transformation of the mixed function between these two models was established[18].

The mathematical expressions for SST turbulence models are as follows.

$$\frac{D(\rho k)}{Dt} = \tau_{ij}\frac{\partial u_i}{\partial x_j} - \beta^*\rho k\omega + \frac{\partial}{\partial x_j}\left(\Gamma_k \frac{\partial k}{\partial x_j}\right) \tag{6}$$

$$\frac{D(\rho\omega)}{Dt} = \frac{\gamma}{\nu_t}\tau_{ij}\frac{\partial u_i}{\partial x_j} - \beta\rho\omega^2 + \frac{\partial}{\partial x_j}\left(\Gamma_\omega \frac{\partial \omega}{\partial x_j}\right) + 2\rho(1-F_1)\sigma_{\omega,2}\frac{1}{\omega}\frac{\partial k}{\partial x_j}\frac{\partial \omega}{\partial x_j} \tag{7}$$

The expression of the shear stress τ_{ij} is as follows.

$$\tau_{ij} = \mu_t\left(\frac{\partial u_i}{\partial x_j} + \frac{\partial u_j}{\partial x_i} - \frac{2}{3}\frac{\partial u_k}{\partial x_k}\delta_{ij}\right) - \frac{2}{3}\rho k\delta_{ij}. \tag{8}$$

In formula (6), δ_{ij} is the Kronecker function[19].

$$\delta_{ij} = \begin{cases} 1 & i = j \\ 0 & i \neq j \end{cases}, \tag{9}$$

In formula (4) and (5), $\tau_{ij}\frac{\partial u_i}{\partial x_j}$ can be expressed as,

$$\tau_{ij}\frac{\partial u_i}{\partial x_j} = \mu_t\left[s_{ij}^2 - \frac{2}{3}\left(\frac{\partial u_k}{\partial x_k}\right)^2\right] - \frac{2}{3}\rho k\frac{\partial u_k}{\partial x_k}, \tag{10}$$

In formula (10),

$$s_{ij} = \frac{\partial u_i}{\partial x_j} + \frac{\partial u_j}{\partial x_i} \tag{11}$$

In formula (6) and (7), Γ_k and Γ_ω represent the effective diffusion term of the k and ω respectively, $\beta^*\rho k\omega$ and $\beta\rho\omega^2$ represents the divergence term respectively. The last item of formula (7) represents an orthogonal divergence term.

The equations of the effective diffusion term,

$$\Gamma_\omega = \mu + \sigma_\omega \mu_t, \tag{12}$$

$$\Gamma_k = \mu + \sigma_k \mu_t, \tag{13}$$

$$\sigma_k = F_1 \sigma_{k,1} + (1 - F_1)\sigma_{k,2}, \tag{14}$$

$$\sigma_\omega = F_1 \sigma_{\omega,1} + (1 - F_1)\sigma_{\omega,2}. \tag{15}$$

The switching function F_1 is expressed as follows,

$$F_1 = \tanh\left(\theta_1^4\right), \tag{16}$$

$$\theta_1 = \min\left[C, \frac{4\sigma_{\omega,2}\rho k}{D^+ y^2}\right], \tag{17}$$

$$C = \max\left(\frac{\sqrt{k}}{0.09\omega y}, \frac{500\nu}{y^2\omega}\right), \tag{18}$$

$$D^+ = \max\left(\frac{2\rho\sigma_{\omega,2}}{\omega}\frac{\partial k}{\partial x_j}\frac{\partial \omega}{\partial x_j}, 10^{-20}\right). \tag{19}$$

In formula (14) and (15), y is the shortest distance from the current point to the physical plane, D^+ is the positive direction of the orthogonal divergence term.

The function expression of the SST turbulence model, $k-\omega$ turbulence model and standard $k-\varepsilon$ turbulence model are ϕ 、 ϕ_1 and ϕ_2, respectively, the function relation between the three is as follow,

$$\phi = F_1 \phi_1 + (1 - F_1)\phi_2. \tag{20}$$

When ϕ_1 approaching to 0, F_1 is close to 0 also. At this time, the turbulence model applied in this zone is the standard $k-\varepsilon$ model and the constant values are shown in the Table 1[20].

Table1. Constant value in standard $k-\varepsilon$ model.

$\sigma_{k,1} = 0.85$	$\sigma_{k,2} = 1.0$	$\sigma_{\omega,1} = 0.5$
$\sigma_{\omega,2} = 0.856$	$\alpha_1 = 0.31$	$\beta^* = 0.09$
$\kappa = 0.41$	$\beta_{i,1} = 0.075$	$\beta_{i,2} = 0.0828$

$$\gamma_1 = \beta_{i,1}/\beta^* - \sigma_{\omega,1}\kappa^2/\sqrt{\beta^*} \tag{21}$$

$$\gamma_2 = \beta_{i,2}/\beta^* - \sigma_{\omega,2}\kappa^2/\sqrt{\beta^*} \tag{22}$$

The vortex coefficient is defined as follows,

$$\nu_t = \frac{\alpha_1 k}{\max(\alpha_1\omega, \Omega F_2)}. \tag{23}$$

The formulation of F_2 and θ_2 are expressed as follows.

$$F_2 = \tanh\left(\theta_2^2\right), \tag{24}$$

$$\theta_2 = \max\left(\frac{2\sqrt{k}}{0.09\omega y}, \frac{500\nu}{y^2\omega}\right). \tag{25}$$

When $F_1 = 1$, $\phi = \phi_1$, this is $k-\omega$ turbulence model and the constant values are shown in the Table 2.

Table 2. constant value in $k-\omega$ turbulence model[20].

$\sigma_{k,1} = 0.5$	$\sigma_{\omega,1} = 0.5$	$\beta_{i,1} = 0.075$
$\beta^* = 0.09$	$\gamma_1 = 5/9$	$\nu_t = k/\omega$

3.2 Internal flow simulations

In order to fully understand the constraint abrasive jet flow, the internal flow of the tool was calculated firstly, the exit velocity and the pressure of the internal flow were acquired as the initial parameters of the jet, and then the jet was simulated to explain the principle and material removal mechanism of the strongly-constrained AJP based on the fluid mechanics.

The meshes of the internal flow are shown in Figure 4. As the polishing head was an axisymmetric cylindrical head, only one eighth of the flow field was calculated. The lifting height is set as 1.5 mm and the length of the total channel is set as 40 mm.

The meshes were divided by ICEM CFD software. The effect of mesh quality on the convergence of simulation results is considered. The hexahedral meshing was adopted and the top-down "sculpture" grid division method was used, multiple topological blocks of the structure grid can generate. The high quality "O", "C", "L" - shaped hexahedral meshes were gotten and the local grids were refined in the nozzle part. The total number of grids is 57915 after optimizing. The initial parameters listed as follow. In order to observe the changes in pressure and velocity along the flow direction of the abrasive flow, a detection line was set during the simulation, as shown in Figure 5.

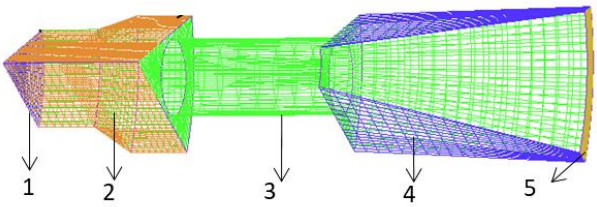

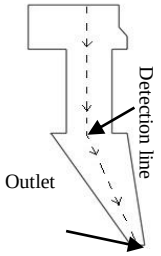

1. Inlet; 2. Periodic symmetric boundary; 3 Division column; 4 Outlet

Figure 4. Simulation model and meshes of the internal flow. **Figure 5.** Detection line.

The pre-loaded force was 128.88 N, the inlet was set as a velocity inlet and the initial velocity was set as 6 m/s. The outlet was set as outflow; the split surfaces of the simulation model were set as periodic symmetric boundary; other sides were set as wall. The pressure distribution and velocity vectors are shown in Figure 6 and Figure 7. The pressure and velocity change with the flow direction are shown in Figure8.

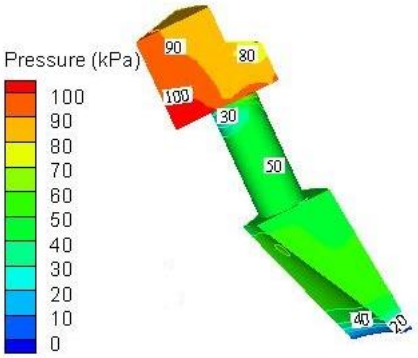

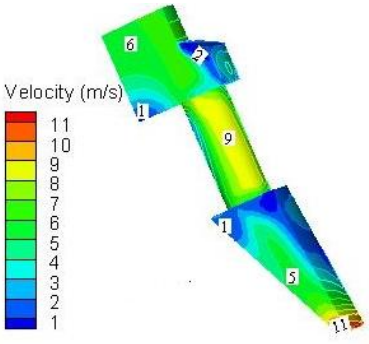

Figure 6. Pressure distribution of internal flow. **Figure 7.** Velocity vectors of internal flow.

Simulation results indicated that the diversion column will increase the abrasive flow velocity and reduce the decrease of the abrasive flow pressure. It was observed that the velocity in the slit exit increased to approximately 11 m/s immediately, with an initial velocity of 6 m/s, which direction is along the tangent of the bottom surface of the polishing tool. This indicated that the C-AJP exhibited a high-energy utilization efficiency compared to a traditional AJP.

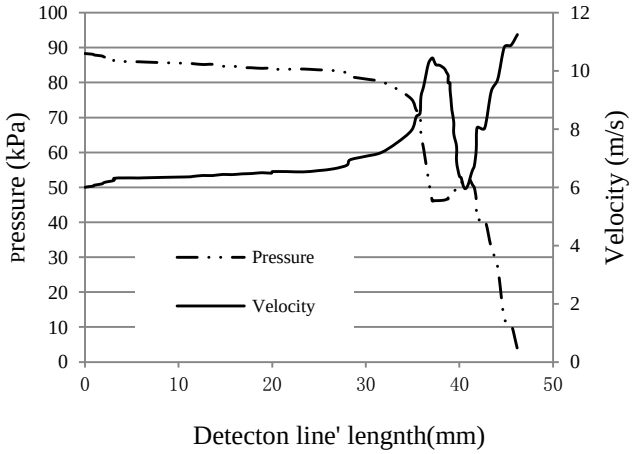

Figure8. Pressure and velocity change along the flow direction.

If the lifting height changed, the out pressure and velocity were changed also, which influenced the out jet flow. The lifting height were set as 1mm,1.5mm, 2mm and 2.5mm, at the same time, the simulation result of the internal flow was shown as table 3.

Table 3. Out pressure and velocity of vary exit slit.

exit slit (mm)	out velocity (m/s)	out pressure (kPa)
1	15	90
1.5	11	50
2	9	30
2.5	8	15

3.3 The surface jet simulation

The abrasive jet with the Novel Nozzle parallel to the workpiece surface is a kind of planar slit jet. According to the above calculation results and empirical formulas of the slit jet, the lengths of the main jet segment was less than 15 mm and the width b was less 10 mm. The nozzle was the center point, so the length of the simulation model for the out jet was set as 30 mm, double the s. The out part of the nozzle was set as inlet of the jet simulation model. The simulation model and meshes of the strong-constraint jet are shown in Figure 9.

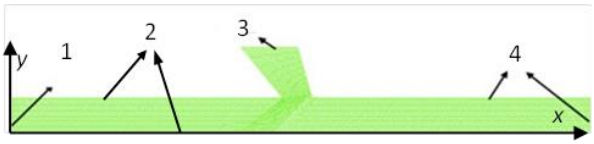

1 Periodic symmetric boundary; 2 Wall; 3 Inlet; 4 Outlet

Figure. 9 Simulation model and meshes of the jet

The initial velocity of the out jet was set as 8m/s, 9m/s, 11 m/s and 15m/s respectively, that calculated by the internal abrasive flow. The pressure distribution of the jet is presented in Figure 10. The pressure decreases significantly in the connecting part of the nozzle and the outlet, but which increases near the wall (work pieces) region. Then the pressure changed little when the length of the jets larger than 5 mm (X coordinates >20 mm) (see Figure 12). The inclined wall of the nozzle decreases the normal pressure of the abrasive flow in the centre region. So the work region of the jet has a stability tangential stress.

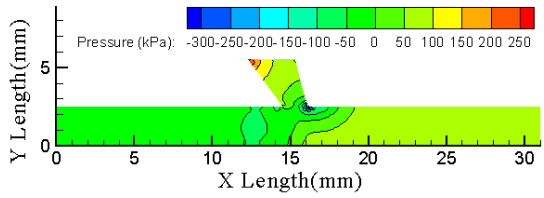

(a) Initial velocity was 8m/s

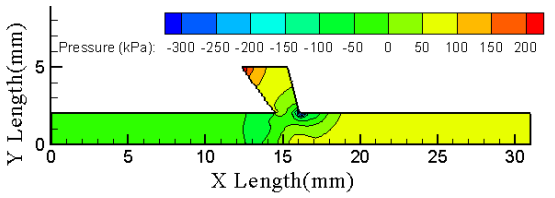

(b) Initial velocity was 9m/s

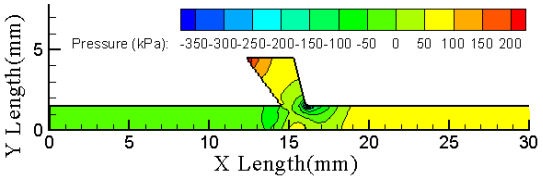

(c) Initial velocity was 11m/s

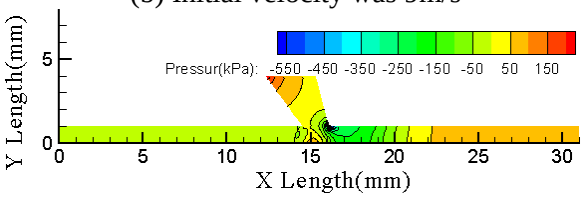

(d) Initial velocity was 15m/s

Figure.10 Pressure distribution of jet.

The velocity vector of the main jet segment was magnified and was shown in Figuree11. The velocity vectors increases significantly in the connecting part of the nozzle and the outlet, but which reduces to a stable value (about 10 m/s) near the wall region where 16 mm <X coordinates <19 mm. Although the velocity vectors inject the work pieces at an angel, the jet direction was changed near the wall which almost paralleled to the surface of the work piece. So this segment is the main work region. Then the velocity vector reduces to 2 m/s or smaller when the length of the jet s was larger than 5 mm (X coordinates>20 mm). The velocity vectors decreased near the surface of the work pieces where 14.5 mm < X coordinates <16 mm. This segment is the centre region of the nozzle with smaller velocity and a relative stability pressure, so it's a second work region. If the lifting height is larger than 2.5mm (include 2.5mm), the velocity vectors near the surface of work piece decrease drastically. The abrasive flow almost no longer has processing capacity.

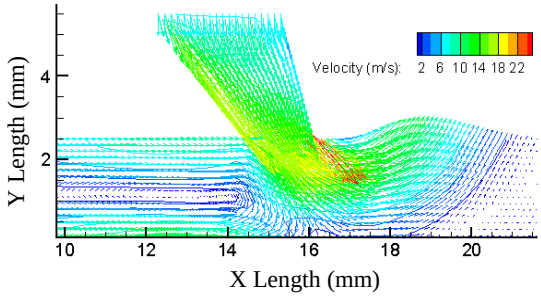

(a) Initial velocity was 8m/s

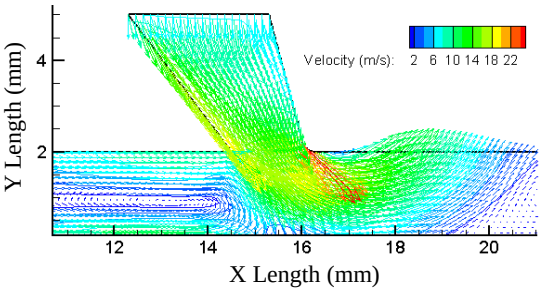

(b) Initial velocity was 9m/s

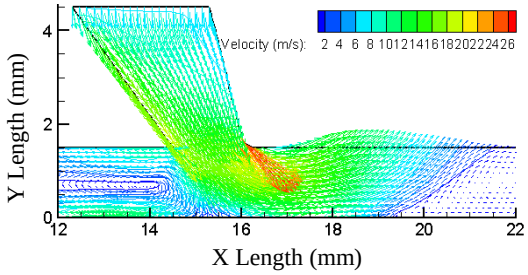

(c) Initial velocity was 11m/s

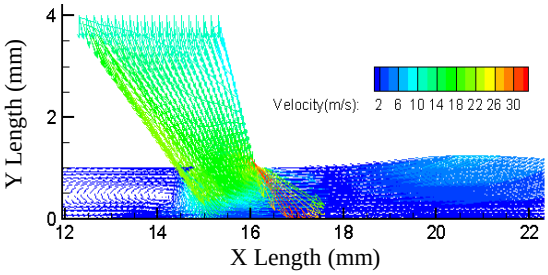

(d) Initial velocity was 15m/s

Figure. 11 Magnified velocity vectors of abrasive jet.

By comparing the simulation results to the theoretical calculation results of the plane slit jet, some difference was seen, indicating that this was a new kind of jet.

The changing trend of the average velocity of the jet with different lifting height was shown in Figure12. The changing trend of average pressure of the jet with different lifting height of the polishing head was shown in Figure 13.

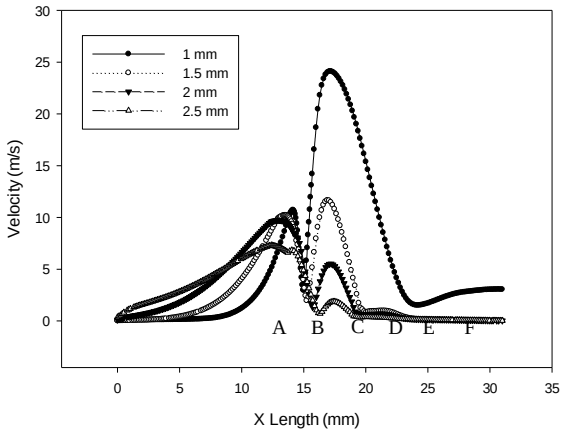

Figure12. The changing trend of average velocity.

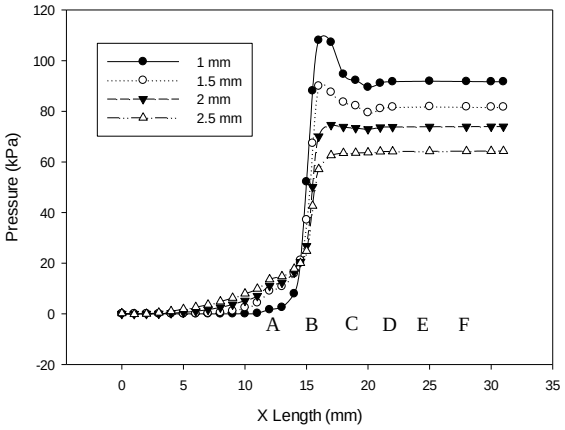

Figure13. The changing trend of average pressure.

As the x-coordinate of the nozzle is 15mm, the part of the x-coordinates greater than 15 mm is the work region. In this region, the velocity vector of the abrasive flow increases rapidly firstly and then decreases close to 0 if the lifting height of the polishing head is unchanged (see Figure 12). If the lifting height of the polishing head is decreased, the peak value of the velocity and the polishing region are increased too. As the part of the X-coordinates less than 15 mm isn't work region, so the changing trend of the velocity vector in this part meant nothing.

The changing trend of the average pressure is like a step-function signal (see Figure 13). The pressure increases suddenly in the connecting part of the outlet and nozzle, then decreases to a stable value if the lifting height of the polishing head is unchanged. If lifting height of the polishing head is decreased, the peak value of the pressure is increased, and the polishing region is increased also.

4 Experiments

A polishing experiment platform, as shown in Figure 14, was built combining the existing high-precision Motorman HP 20 in the laboratory. The polishing tool was drive by the robot manipulator arm (Motorman HP20) and moved according to the planned path defined in advance. The workpiece was revolved with the pan on the rotational table, and the abrasive jet injected from the nozzle along the redial direction on the workpiece surface. Therefore the trajectory paths of abrasives on the workpiece surface are the combination of the motions mentioned above.

The polishing experiments were performed on K9 optical glass, a typical hard and brittle material. In order to observe the nozzle performance, the sample on the table keeps stationary. There are 6 check points on the sample were recorded before and after polishing. The position of the first check point in the middle of the exit section (marked as A in Figures 12 and 13) and the interval between two consecutive check points is 3 mm which along the radial direction. The polishing head was preloaded by the motor control system. The flow parameters of the jet were decided by the lifting height of the polishing head that controlled by the linear stepping motor.

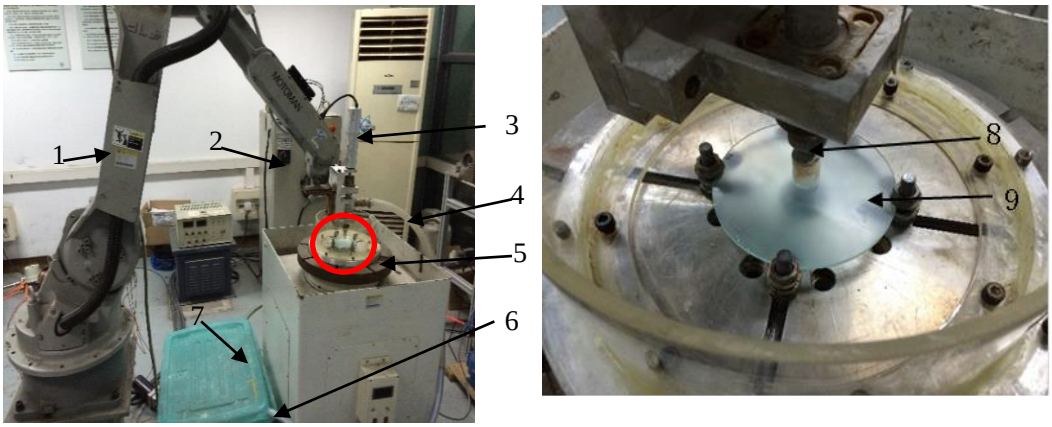

1. Manipulator, 2. Control cabinet, 3. Control motor, 4. Feeding pipe, 5. Processing platform, 6. Return pipe, 7. Grinding box, 8. Touching nozzle, 9. Workpiece.

Figure14. The polishing equipment.

The key processing parameters are shown in Table 4. The abrasive particle material is alumina, the fluid of used for the abrasive jet was de-ionized water and the inlet flow pressure was set as 0.172MPa. The K9 glass was processed in the experiments. After 4 hours of processing, the material removal volume at each selected point was measured in the value of removal depth (μm). The removal depth variation with test points was shown in Figure 15.

Table 4. Experimental parameters.

Experimental control factors	Factor value
abrasive	alumina
Polishing gap	1 mm
abrasive size	10 μm
abrasive concentration	15%
Additives and concentrations	0.1% Zinc nitrate

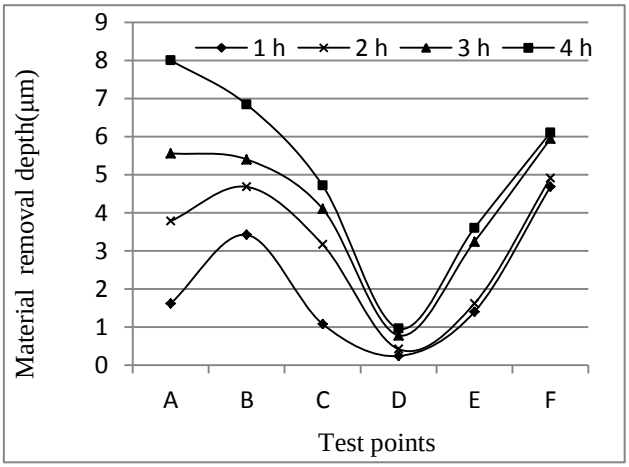

Figure15. Removal depth change with the test points.

As shown in Figure 15, the material removal volume at the point A is the largest and at the point D is the smallest after polishing 4 hours. Compare to the simulation results in Figure 10 to Figure 13, the pressure of point A is the largest although the velocity is low. The velocity and pressure of point D is the lowest. According to the Preston formula, the material removal volume is positively correlated with the velocity and pressure[21].

$$\nabla z = \int_0^t k_p v p dt, \quad (26)$$

The material removal volume at point B is the second largest, even larger than the first point at the beginning of polishing. Compare to the Figure 12 and 13, the pressure of point B is lower than point A, but the velocity is much higher than point A. In order to achieve uniform polishing, the polishing time at different positions needs to be set according to the material removal rate.

The surface roughness change with the test point was shown in Figure 16. The surface roughness at the point A, B and C improving with time is very significant, and all decrease with polishing time. The decrease of surface roughness at point B is most pronounced. At the point D, although the surface roughness of the workpiece has a tendency to decrease at a small scale, the reduction is much less than that of the point A, B and C. At the point E and F, the roughness of the workpiece surface did not improve, instead it increased significantly.

As the point A located in the middle of the nozzle exit section where the jet transfer from normal to tangential, the normal pressure is high, but the velocity is low, so the normal impact results in material removal mainly rather than damage surface. This makes the material removal volume the largest and the surface roughness only a bit worse than the point B.

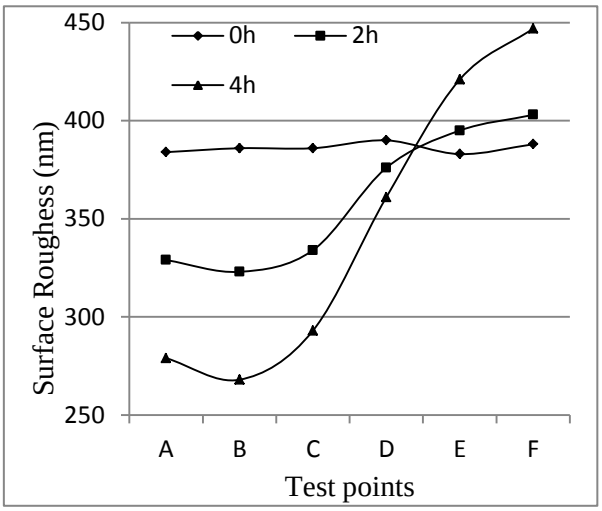

Figure16. Surface roughness change with the test points.

The simulation results of the velocity (in Figure 11) shown that the jet at the point B almost parallel to the workpiece surface, the tangential force of the jet reaches the maximum value and the velocity is almost the peak, the surface roughness decreased obviously. So material removal caused by tangential force is the main way to reduce surface damage. Comprehensive consideration of material removal volume and surface roughness, the processing performance at the point B is the best.

Similar to check point B, the tangential force component on check point C is still larger, so it shows good processing results too. The point D could be considered as the end of effective polishing range of the jet, so the removal volume is low and the surface roughness changes are small.

The simulation of velocity (in Figure 12) shown that the velocity has increased and presented a vortex pattern from the point E. On the other hand, since the workpiece is curved, the angle of incidence is increased with the distance from the ejection point, the normal impact increased which cause several scratches along the radial direction on the surface, resulting in the surface roughness is increased in spite of the material removal volume is high.

5 Conclusions

(1) The simulation of the internal flow shown that the jet velocity increased with the decrease of the slit gap between the bottom surface of the polishing tool head and the surface of the workpiece. And the pressure loss of the abrasive jet induced by the gap is immense. In order to ensure processing efficiency, the gap should be as small as possible.

(2) It was concluded that the abrasive flow velocity at the nozzle exit were parallel to the workpiece. Compared to a traditional AJP, it not only solved the divergence of the jet beam, but also made the abrasive particles move along the workpiece's surface, strengthening the shearing action of the polishing abrasive and reducing the normal impact of the abrasive.

(3) The experimental material removal volume and the surface roughness of the workpiece surface were observed and the results illustrated that the polishing mechanism of the AJP with the new nozzle mainly relied on the shearing actions of the jet and the effective polishing distance of the jet is obtained. In order to balance polishing efficiency and impact damage, it is necessary to set different polishing time according to different polishing positions.

Acknowledgements

This work was supported by the NNSF of China (Grant No. 51305399)

References

[1]. Zhao, Qingliang, Yingchun Liang, David Stephenson, et al., 2007,Surface and subsurface integrity in diamond grinding of optical glasses on Tetraform 'C' *International journal of machine tools & manufacture*. **47**(14) p. 2091-2097.

[2]. Zhao, Qingliang and Bing Guo, 2015,Ultra-precision grinding of optical glasses using mono-layer nickel electroplated coarse-grained diamond wheels. Part 1: ELID assisted precision conditioning of grinding wheels *Precision engineering*. **39** p. 56-66.

[3]. Harvey, J. E., K. L. Lewotsky, and A. Kotha, 1995,Effects of surface scatter on the optical performance of x-ray synchrotron beam-line mirrors *Appl Opt*. **34**(16) p. 3024.

[4]. M., Hashish, 1992,Diamond film polishing with abrasive-liquid jets: an exploratory investigation. American Society of Mechanical Engineers, Production Engineering Division. **58** p. 29- 41.

[5]. Ansari, A. I. and M. Hashish, 1995,Effect of abrasive waterjet parameters on volume removal trends in turning *Journal of Engineering for Industry-Transactions of the Asme*. **117**(4) p. 475-484.

[6]. Fähnle, O. W., H. Brug, and H. J. Frankena, 1998,Fluid jet polishing of optical surfaces *Appl Opt*. **37**(28) p. 6771.

[7]. Faehnle, Oliver W. and Hedser H. van Brug, 1999 Fluid jet polishing: removal process analysis. SPIE. p. 68-77.

[8]. Booij, Silvia M., Oliver W. Fähnle, and Joseph J. M. Braat, 2004,Shaping with fluid jet polishing by footprint optimization *Appl Opt*. **43**(1) p. 67.

[9]. Booij, Silvia M., Hedser van Brug, Joseph J. M. Braat, et al., 2002,Nanometer deep shaping with fluid jet polishing *Optical Engineering*. **41**(8) p. 1926-1931.

[10]. Messelink, Wilhelmus A. C. M., Reto Waeger, Torsten Wons, et al., 2005 Prepolishing and finishing of optical surfaces using fluid jet polishing. SPIE. p. 586908-586906.

[11]. Matsumura, T., T. Muramatsu, and S. Fueki, 2011,Abrasive water jet machining of glass with stagnation effect *CIRP annals*. **60**(1) p. 355-358.

[12]. Kalirasu, S., N. Rajini, S. Rajesh, et al., 2017,AWJM Performance of jute/polyester composite using MOORA and analytical models *Materials and manufacturing processes*. **32**(15) p. 1730-1739.

[13]. Anand, Umang, 2002 Prevention of nozzle wear in abrasive water suspension jets (AWSJ) using porous lubricated nozzles. ProQuest Dissertations Publishing.

[14]. Nanduri, Madhusarathi, David G. Taggart, and Thomas J. Kim, 2002,The effects of system and geometric parameters on abrasive water jet nozzle wear *International journal of machine tools & manufacture*. **42**(5) p. 615-623.

[15]. Ngoc Pi Vu, Nguyen Quoc Tuan, 2009,A study on nozzle wear modeling in abrasive water jet cutting *Advanced Materials Research*. **76** p. 345–350.

[16]. Menter, F.R.,1992 *Improved Two-equation K-omega Turbulence Models for Aerodynamic Flows*.

[17]. Menter, F. R., 1994,Two-equation eddy-viscosity turbulence models for engineering applications *AIAA Journal*. **32**(8) p. 1598-1605.
[18]. Ansari, M., M. R. H. Nobari, and E. Amani, 2019,Determination of pitch angles and wind speeds ranges to improve wind turbine performance when using blade tip plates *Renewable energy*. **140** p. 957-969.
[19]. Matthes, Nils, 2019,An algebraic characterization of the Kronecker function *Research in the Mathematical Sciences*. **6**(3) p. 1-13.
[20]. Matyushenko, A. A. and A. V. Garbaruk, 2016,Adjustment of the k-ω SST turbulence model for prediction of airfoil characteristics near stall *Journal of Physics: Conference Series*. **769** p. 012082.
[21]. Ji, Shiming, 2011,Study on Machinability of Softness Abrasive Flow Based on Preston Equation *Ji xie gong cheng xue bao*. **47**(17) p. 156.